





## Article

# Hydrogen and Oxygen Evolution on Flexible Catalysts Based on Nickel–Iron Coatings

Dmytro Shyshkin <sup>1,2</sup>, Loreta Tamašauskaitė-Tamašiūnaitė <sup>1,\*</sup> , Dijana Šimkūnaitė <sup>1</sup>, Aldona Balčiūnaitė <sup>1</sup>, Zita Sukackienė <sup>1</sup> , Jūratė Vaičiūnienė <sup>1</sup>, Birutė Šimkūnaitė-Stanyrienė <sup>1</sup>, Antanas Nacys <sup>1</sup> , and Eugenijus Norkus <sup>1</sup> 

<sup>1</sup> Department of Catalysis, Center for Physical Sciences and Technology (FTMC), LT-10257 Vilnius, Lithuania; dmytro.shyshkin@ftmc.lt (D.S.); dijana.simkunaite@ftmc.lt (D.Š.); aldona.balciunaite@ftmc.lt (A.B.); zita.sukackiene@ftmc.lt (Z.S.); jurate.vaiciuniene@ftmc.lt (J.V.); birute.simkunaite@ftmc.lt (B.Š.-S.); antanas.nacys@ftmc.lt (A.N.); eugenijus.norkus@ftmc.lt (E.N.)

<sup>2</sup> Faculty of Chemistry and Geosciences, Vilnius University, LT-03225 Vilnius, Lithuania

\* Correspondence: loreta.tamasauskaite@ftmc.lt

**Abstract:** The electrolysis of water is one of low-cost green hydrogen production technologies. The main challenge regarding this technology is designing and developing low-cost and high-activity catalysts. Herein, we present a strategy to fabricate flexible electrocatalysts based on nickel–iron (NiFe) alloy coatings. NiFe coatings were plated on the flexible copper-coated polyimide surface (Cu/PI) using the low-cost and straightforward electroless metal-plating method, with morpholine borane as a reducing agent. It was found that Ni<sub>90</sub>Fe<sub>10</sub>, Ni<sub>80</sub>Fe<sub>20</sub>, Ni<sub>60</sub>Fe<sub>40</sub>, and Ni<sub>30</sub>Fe<sub>70</sub> coatings were deposited on the Cu/PI surface; then, the concentration of Fe<sup>2+</sup> in the plating solution was 0.5, 1, 5, and 10 mM, respectively. The morphology, structure, and composition of Ni<sub>x</sub>Fe<sub>y</sub>/Cu/PI catalysts have been examined using scanning electron microscopy (SEM), energy-dispersive X-ray spectroscopy (EDX), X-ray diffraction (XRD), and inductively coupled plasma–optical emission spectroscopy (ICP-OES), whereas their activity has been investigated for hydrogen evolution (HER) and oxygen evolution (OER) reactions in 1 M KOH using linear sweep voltammetry (LSVs). It was found that the Ni<sub>80</sub>Fe<sub>20</sub>/Cu/PI catalyst exhibited the lowest overpotential value of −202.7 mV for the HER, obtaining a current density of 10 mA cm<sup>−2</sup> compared to Ni<sub>90</sub>Fe<sub>10</sub>/Cu/PI (−211.9 mV), Ni<sub>60</sub>Fe<sub>40</sub>/Cu/PI (−276.3 mV), Ni<sub>30</sub>Fe<sub>70</sub>/Cu/PI (−278.4 mV), and Ni (−303.4 mV). On the other hand, the lowest OER overpotential (344.7 mV) was observed for the Ni<sub>60</sub>Fe<sub>40</sub>/Cu/PI catalyst, obtaining a current density of 10 mA cm<sup>−2</sup> compared to the Ni<sub>35</sub>Fe<sub>65</sub> (369.9 mV), Ni<sub>80</sub>Fe<sub>20</sub> (450.2 mV), and Ni<sub>90</sub>Fe<sub>10</sub> (454.2 mV) coatings, and Ni (532.1 mV). The developed Ni<sub>60</sub>Fe<sub>40</sub>/Cu/PI catalyst exhibit a cell potential of 1.85 V at 10 mA cm<sup>−2</sup>. The obtained catalysts seem to be suitable flexible catalysts for HER and OER in alkaline media.

**Keywords:** nickel; iron; morpholine borane; electroless metal plating; water splitting; hydrogen evolution; oxygen evolution



**Citation:** Shyshkin, D.; Tamašauskaitė-Tamašiūnaitė, L.; Šimkūnaitė, D.; Balčiūnaitė, A.; Sukackienė, Z.; Vaičiūnienė, J.; Šimkūnaitė-Stanyrienė, B.; Nacys, A.; Norkus, E. Hydrogen and Oxygen Evolution on Flexible Catalysts Based on Nickel–Iron Coatings. *Catalysts* **2024**, *14*, 843. <https://doi.org/10.3390/catal14120843>

Academic Editor: Luca Gonsalvi

Received: 14 October 2024

Revised: 6 November 2024

Accepted: 20 November 2024

Published: 22 November 2024



**Copyright:** © 2024 by the authors. Licensee MDPI, Basel, Switzerland. This article is an open access article distributed under the terms and conditions of the Creative Commons Attribution (CC BY) license (<https://creativecommons.org/licenses/by/4.0/>).

## 1. Introduction

The search for novel and optimized energy storage and usage technologies is accelerating rapidly. In order to be considered for implementation, these technologies must satisfy three principal criteria: they must be efficient, reliable, and inexpensive. Among these technologies, electrochemical energy is emerging as a clear front-runner, offering significant potential for advancement. The production of clean hydrogen via electrolytic water splitting represents a viable and efficient approach, with hydrogen being considered an optimal substitute for traditional fossil fuels [1–3]. The electrochemical water splitting process involves two half-reactions: the hydrogen evolution reaction (HER), which occurs at the cathode, and the oxygen evolution reaction (OER), which occurs at the anode electrode. The slow kinetics of these reactions represent a significant challenge that must be

addressed. The efficiency of this process can be markedly enhanced through the strategic use of carefully selected catalysts, including various metal-based catalysts, perovskite oxides, etc. [4,5]. Advancements in electrocatalysts, in particular those with reduced overpotential and enhanced durability, have the potential to contribute to an improvement in the efficiency of HER/OER processes. Precious metal-based materials, such as Pt for HER and Ir/RuO<sub>x</sub> or their alloys for OER, have been identified as the most effective catalysts for water splitting [6–10]. However, there are still some challenges to be addressed, particularly in terms of cost and availability, which could affect their large-scale applications.

A variety of non-noble transition metal-based (TM) catalysts has been developed as an alternative to the high-cost but effective noble metal-based catalysts [11–13]. Systems, based on iron and nickel, have been demonstrated to have considerable potential for the overall splitting of water. For example, heterostructures of Fe-Ni<sub>3</sub>S<sub>2</sub>/Ni<sub>12</sub>P [14], Fe-doped nickel-based phosphides [15], Ni/NiFe-Pyro@IF [16], and amorphous Ni-Fe-P alloys with varying phosphorous concentrations [17] have demonstrated impressive electrocatalytic activity with respect to both the OER and HER processes. However, the intrinsic electrocatalytic effectiveness of the majority of current catalysts has yet to be fully realized, primarily due to a number of challenges, including low activity, low conductivity, poor stability, and high aggregation. The electrochemical performance of Ni-Fe catalysts has been enhanced on numerous occasions through the utilization of non-metallic elements, including sulfur [18], phosphorus [18], boron [19], and selenium [20], among others. The incorporation of additional heteroatoms with varying atomic radius and electronegativities into the catalyst can lead to further changes in the electronic structure of the material surface, thereby speeding the overall water-splitting process [17].

In many cases, the selection of an appropriate substrate represents a key strategy for enhancing catalyst performance. For example, the use of high-conductive nickel [21,22], iron [16], or both nickel–iron [18,23] foams not only improves the conductivity of the material, but also significantly increases the electrochemically active surface area of the catalyst. Furthermore, cost-effective carbon-based substrates, including carbon cloth [24,25], carbon nanotubes (CNTs) [25], carbon nitrides [26], graphitic carbon [27], and graphite felt [28], can also be employed for this purpose. However, the use of unmodified pristine carbonaceous materials has been observed to result in reduced activity, particularly at the anodic reaction, due to their susceptibility to oxidative degradation at higher anodic polarizations. On the other hand, CNTs, graphene, conductive polymers, Si or Ag nanofibers, and carbon cloth, which have a high specific surface area and a high electrical conductivity, are used in the design and development of flexible devices, including flexible solar cells, flexible lithium batteries, flexible supercapacitors, flexible proton-exchange membrane fuel cells (PEMFCs), and PEM electrolyzers, which have attracted considerable attention due to a number of advantages including their flexibility, shape versatility, low weight, and excellent mechanical properties [29]. It is important that the flexible electrodes have excellent flexibility, high stability, and high gas permeability. In addition, the catalyst deposited on the flexible substrate should have high electrical conductivity as well as a high adhesion of the catalyst to the substrate.

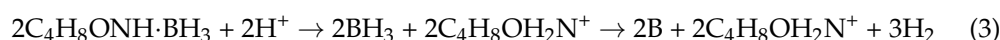
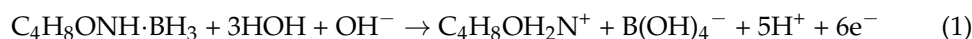
In such circumstances, polyimide (PI), which represents a class of conducting polymers, emerges as a potentially more suitable candidate for the substrate due to its favorable electronic conductivity, excellent oxidative stability in both strong acids and alkalis, flexibility, and low cost [30]. Recently, the polyimide–carbon nanotube (PI-CNT) film has been referenced as a promising substrate for a flower-like Co-Ni alloy catalyst, which has demonstrated a notable enhancement in the catalyst's OER performance. This was characterized by a low overpotential and a rapidly increasing current density [31]. Another high-performing OER catalyst was developed by immobilizing iridium (Ir) single atoms on a PI support, exhibiting high mass activity on a carbon paper electrode while simultaneously achieving outstanding stability with negligible decay for 360 h [32]. Furthermore, a reduced graphene oxide–polyimide/carbon nanotube film decorated with NiSe nanoparticles was used directly as a HER electrocatalyst without further treatments, which exhibited

well-defined HER catalytic activity [33]. Meanwhile, FeNi<sub>3</sub>/Fe<sub>3</sub>O<sub>4</sub> hybrid NPs anchored to laser-induced graphene (LIG) electrodes directly patterned on both sides of an inexpensive polyimide film showed exceptional performance in water splitting [34].

It is important to note that using polyimide supports can help overcome the limitations associated with polymeric binders like Nafion, which are typically required for TM-based catalysts. These limitations include increased electrical resistance, a decreased active area of the catalyst, and the reduced efficiency of electrocatalyst binding to the conductive support [35]. Typically, fine-grained catalytic NPs are mixed with a polymer binder (Nafion), conductive fillers, and a solvent to form an ink, and then sprayed onto the conductive electrodes. From this point of view, PI supports can facilitate a more even distribution of catalysts, avoiding the sparse accumulation often observed when using traditional methods like spraying ink mixtures onto conductive electrodes. It is therefore of particular importance to consider the use of PI supports for the development of catalysts [30,36]. This work presents a strategy for the fabrication of flexible electrocatalysts based on NiFe alloy coatings on copper-coated low-cost polyimide surfaces (Cu/PI) using a simple and straightforward electroless metal-plating method with the aim of using them as anode/cathode catalysts for hydrogen production by water splitting.

## 2. Results and Discussion

The production of green hydrogen via water electrolysis is widely investigated and the main research is focused on the search and development of an efficient and low-cost materials with high activity for hydrogen and oxygen evolution reactions. Many materials are created, like Pt-based catalysts and non-noble metal catalysts. In this study, we present a strategy to fabricate flexible electrocatalysts based on nickel–iron coatings. We use polyimide coated with a copper film as the flexible substrate. PI is lightweight, flexible, resistant to heat and chemicals. Ni<sub>x</sub>Fe<sub>y</sub> coatings were deposited on the Cu surface by a simple electroless metal-plating method using morpholine borane (MB) as a reducing agent. The reactions occurring during the NiFe coatings deposition are the oxidation of the reducing agent—MB (Equation (1)) and the cathodic reduction in NiFe (Equation (2)) and boron (B) (Equation (3)):

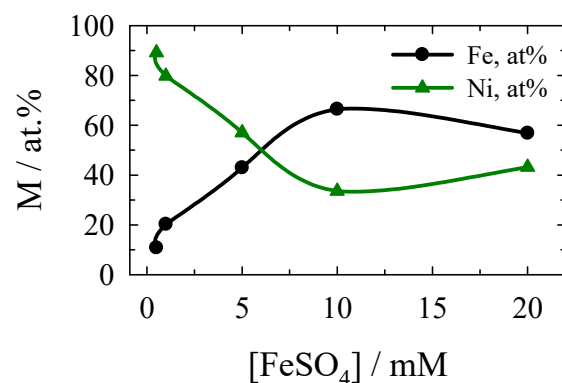


In order to obtain the NiFe coatings with different contents of Ni and Fe, the plating baths were used, where concentrations of glycine, nickel sulfate, ethylenediaminetetraacetic acid, and sodium malonate were kept constant, whereas the concentration of iron sulfate ranged from 0.5 to 10 mM. The plating bath operated at a temperature of 60 °C for one hour. The composition of the coatings was analyzed by ICP-OES. The data obtained are shown in Table 1. By varying the concentration of iron sulfate in the plating bath, we deposited the NiFe coatings with different compositions—the content of Ni varied from 90 to 35 at.% and iron—from 10 to 65 at.%. As can be seen, when Ni<sub>90</sub>Fe<sub>10</sub>, Ni<sub>80</sub>Fe<sub>20</sub>, Ni<sub>60</sub>Fe<sub>40</sub>, and Ni<sub>35</sub>Fe<sub>65</sub> coatings were deposited on the Cu/PI surface, the concentration of Fe<sup>2+</sup> in the plating solution was 0.5, 1, 5, and 10 mM, respectively.

Figure 1 shows the dependence of the deposited Fe and Ni content in the NiFe coatings on the concentration of FeSO<sub>4</sub> in the plating solution. It can be seen that by increasing the Fe<sup>2+</sup> concentration up to 10 mM, the deposited Ni content decreases and the Fe content increases.

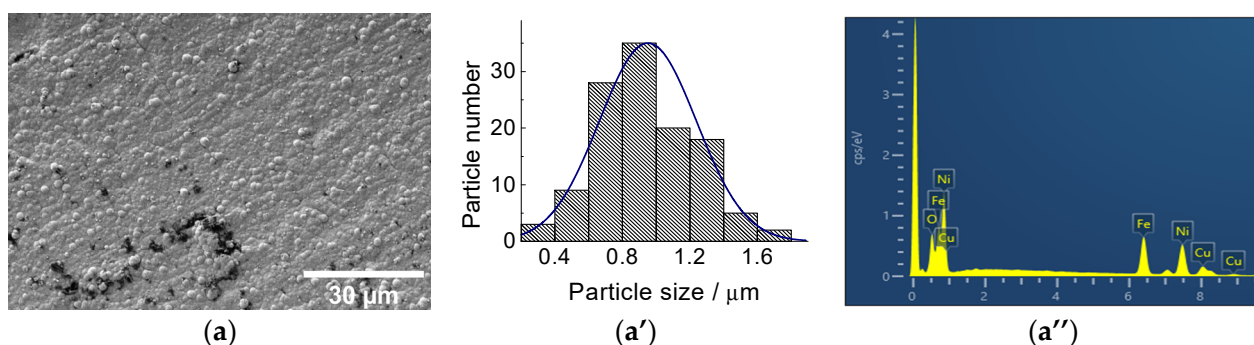
**Table 1.** The composition of the deposited  $\text{Ni}_x\text{Fe}_y$  coatings determined by ICP-OES analysis.

Sample	Metal Loading in the Coatings, $\text{mg cm}^{-2}$			Element, at. %		Coating Denoted as
	Ni	Fe	Ni+Fe	Ni	Fe	
No. 1	0.4805	0.9060	1.3865	34.60	65.30	$\text{Ni}_{35}\text{Fe}_{65}$
No. 2	0.6305	0.4521	1.0826	58.24	41.76	$\text{Ni}_{60}\text{Fe}_{40}$
No. 3	2.9040	0.6995	3.6035	80.60	19.40	$\text{Ni}_{80}\text{Fe}_{20}$
No. 4	2.3400	0.2695	2.6095	89.70	10.30	$\text{Ni}_{90}\text{Fe}_{10}$

**Figure 1.** The content of deposited Fe and Ni in NiFe coatings as a function of the concentration of  $\text{FeSO}_4$  in the plating solution.

In addition, further increases in the  $\text{Fe}^{2+}$  concentration in the plating solution result in lower Fe content and higher Ni content in the NiFe coating. The plating rate for the  $\text{Ni}_{90}\text{Fe}_{10}$ ,  $\text{Ni}_{80}\text{Fe}_{20}$ ,  $\text{Ni}_{60}\text{Fe}_{40}$ , and  $\text{Ni}_{35}\text{Fe}_{65}$  coatings was approximately 2.6, 3.6, 1.1, and  $1.4 \text{ mg cm}^{-2} \text{ h}^{-1}$ , respectively.

The morphology and composition of the  $\text{Ni}_x\text{Fe}_y$  coatings were characterized using SEM and EDX analysis (Figure 2). The SEM images show that the  $\text{Ni}_x\text{Fe}_y$  coatings are compact, smooth, and free of cracks (Figure 2a–d). The  $\text{Ni}_x\text{Fe}_y$  coatings have a typical globular morphology consisting of smaller nodules. The average size of the granular nickel–iron particles is approximately 0.8–1.0  $\mu\text{m}$  (Figure 2a'–d'). It is evident that the formation of agglomerates is enhanced by the higher Fe content in the coating, as observed in the  $\text{Ni}_{35}\text{Fe}_{65}$  sample. The energy-dispersive X-ray analysis confirms the presence of nickel and iron in all coatings (Figure 2a''–d'').

**Figure 2.** Cont.



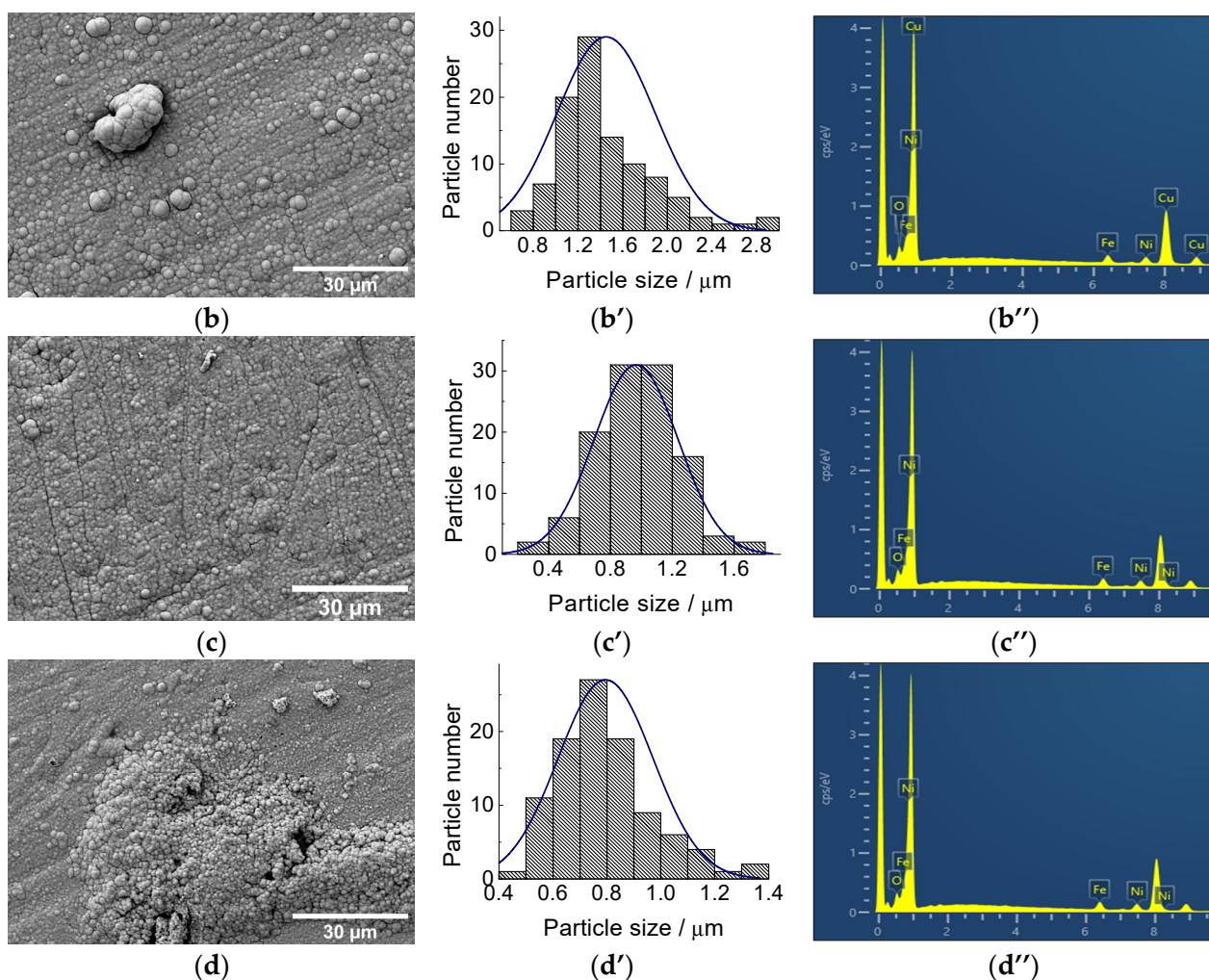


**Figure 2.** The SEM images of  $\text{Ni}_{90}\text{Fe}_{10}$  (a),  $\text{Ni}_{80}\text{Fe}_{20}$  (b),  $\text{Ni}_{60}\text{Fe}_{40}$  (c), and  $\text{Ni}_{35}\text{Fe}_{65}$  (d) coatings, the corresponding particle size distribution (a'–d') and EDX spectra (a''–d'').

The XRD patterns of the  $\text{Ni}_x\text{Fe}_y$  coatings obtained are shown in Figure 3. The peaks at about  $43.6^\circ$ ,  $50.7^\circ$  and  $74.3^\circ$  can be indexed to the (111), (200) and (220) planes of the fcc Fe-Ni alloy (JCPDS card No. 47-1405), respectively (Figure 3) [37]. For example, in the case of  $\text{Ni}_{35}\text{Fe}_{65}$ , with the higher Fe content, the additional peak at  $45.2^\circ$  is seen in the XRD pattern which can be indexed to the (110) plane of the bcc Fe-Ni alloy (JCPDS card no. 37-0474) [38]. It can be seen that between 10 at.% Fe and 40 at.% Fe (Figure 3a–c), the fcc structure predominates, with the presence of the (111), (200) and (220) fcc peaks. Increasing the Fe content up to 65 at.% in the coating results in the appearance of the bcc (110) contribution, while the fcc (111) remains predominant in the XRD pattern (Figure 3d).

Hydrogen evolution was investigated on the obtained catalysts in an  $\text{N}_2$ -deaerated 1 M KOH solution. The HER polarization curves on the different  $\text{Ni}_x\text{Fe}_y/\text{Cu}/\text{PI}$  catalysts are shown in Figure 4a. The data given in Table 2 show that among the investigated catalysts, the lowest onset potential ( $E_{\text{onset}}$ ) of  $-0.0928$  V exhibits the  $\text{Ni}_{80}\text{Fe}_{20}$  catalyst compared to the  $\text{Ni}_{90}\text{Fe}_{10}$ ,  $\text{Ni}_{35}\text{Fe}_{65}$ , and  $\text{Ni}_{60}\text{Fe}_{40}$ . In addition, this catalyst shows the highest current density at  $-0.45$  V (Figure 4a) and the lowest overpotential of  $-202.7$  mV to achieve the current density of  $10 \text{ mA cm}^{-2}$ .

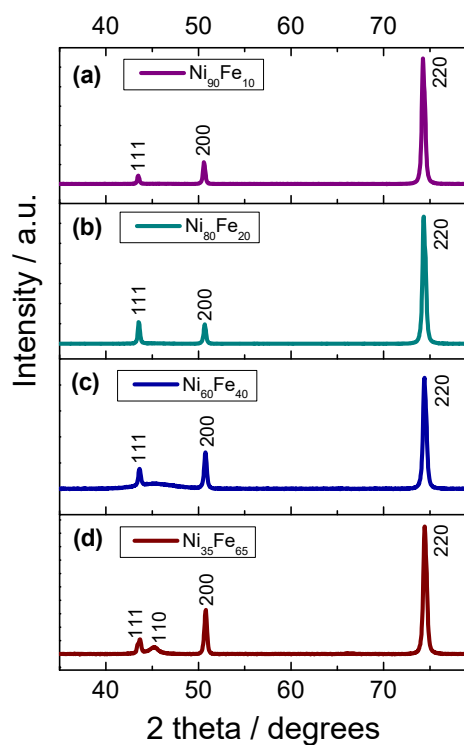


**Figure 3.** XRD patterns of different  $\text{Ni}_x\text{Fe}_y$  coatings:  $\text{Ni}_{90}\text{Fe}_{10}$  (a),  $\text{Ni}_{80}\text{Fe}_{20}$  (b),  $\text{Ni}_{60}\text{Fe}_{40}$  (c), and  $\text{Ni}_{35}\text{Fe}_{65}$  (d).

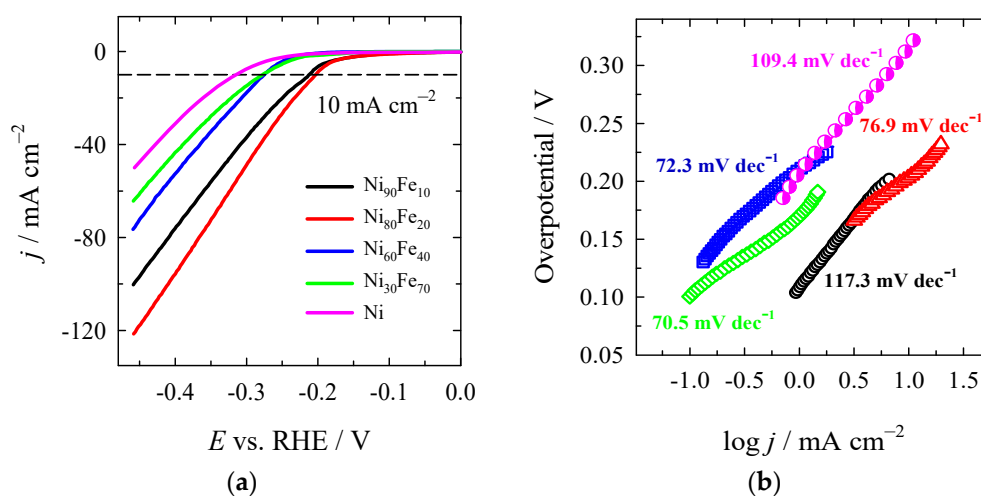


**Figure 4.** (a) HER polarization curves of Ni,  $\text{Ni}_{90}\text{Fe}_{10}$ ,  $\text{Ni}_{80}\text{Fe}_{20}$ ,  $\text{Ni}_{60}\text{Fe}_{40}$ , and  $\text{Ni}_{35}\text{Fe}_{65}$  catalysts in  $\text{N}_2$ -saturated 1 M KOH solution at a potential scan rate of  $2 \text{ mV s}^{-1}$ ; (b) the corresponding Tafel slopes for each catalyst.

The reaction kinetics and mechanism of the as-prepared catalysts can be evaluated based on Tafel slopes determined from the following equation (Equation (4)) [39]:

$$\eta = b \cdot \log j / j_0 \quad (4)$$

$\eta$  is the overpotential,  $b$  is the Tafel slope,  $j$  is the experimental current density, and  $j_0$  is the exchange current density. The plot of  $\eta$  versus  $\log j$  represents the Tafel slope. It is widely accepted that, in alkaline media, the HER mechanism commences with the electrochemical adsorption of a water molecule on the active site of the cathode. This results in the formation of the adsorbed H-species, commonly referred to as the Volmer step. It is followed by two competing reactions that are responsible for the generation of a hydrogen

molecule that leaves the surface. These are the chemical recombination of the adsorbed H (Tafel step) and the electrochemical desorption (Heyrovsky step). Overall, three main steps are involved, as shown in Equations (5)–(7) [40–42]:

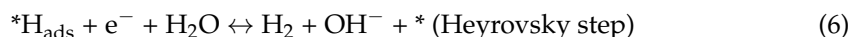


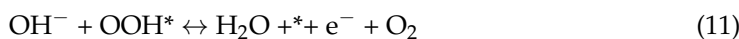
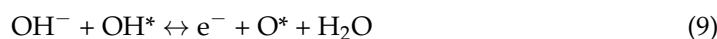
**Table 2.** The electrochemical performance of Ni and the deposited Ni<sub>x</sub>Fe<sub>y</sub> coatings for HER in alkaline media.

Sample	$E_{\text{onset}}$ , V at $j = -1 \text{ mA cm}^{-2}$	$\eta_{10}^*$ , mV	Tafel Slope, $\text{mV dec}^{-1}$
Ni	−0.1722	303.4	109.4
Ni <sub>90</sub> Fe <sub>10</sub>	−0.1081	211.9	117.3
Ni <sub>80</sub> Fe <sub>20</sub>	−0.0928	202.7	76.9
Ni <sub>60</sub> Fe <sub>40</sub>	−0.2113	276.3	72.3
Ni <sub>35</sub> Fe <sub>65</sub>	−0.1710	278.4	70.5

\* Overpotential at 10 mA cm<sup>−2</sup>.

H<sub>ads</sub> denotes the H<sub>2</sub> adsorbed to the metal sites, where \* represents the metal sites. The theoretical Tafel slopes in the aforementioned reaction steps are 120 mV dec<sup>−1</sup>, 40 mV dec<sup>−1</sup>, and 30 mV dec<sup>−1</sup>, respectively. The corresponding Tafel plots for NiFe catalysts are shown in Figure 4b. An increase in the Fe content of NiFe coatings results in a significant reduction in the Tafel slope of 70.5 mV dec<sup>−1</sup>, indicating an increase in the rate control exerted by the Heyrovsky step. However, it is challenging to draw a definitive conclusion about the mechanism based on the determined value, which is not a conventional value for the HER. Based on HER polarization curves in Figure 4a and the Tafel slopes determined, the most promising composition of NiFe is Ni 80 at.% and Fe 20 at.% for efficient HER.

The oxygen evolution reaction in an alkaline medium can be represented by Equations (8)–(11) [41–43]:



where \* denotes the electrocatalyst's adsorption site and, similarly, during OER, the adsorbed intermediates are OH\*, O\*, and OOH\*. The first step of the OER process, denoted by Equation (8), is the electroadsorption of OH<sup>−</sup> onto the active sites of the catalyst's surface. Higher-oxidation-state metal species are more susceptible to the adsorption of OH<sup>−</sup> and the acceleration of the multielectron transportation process, and, hence, can therefore enhance the OER process [44,45]. An OER mechanistic analysis is rather challenging due to its inherent complexity. It involves the transfer of four electrons through different multi-step reaction pathways, which give rise to the formation of a number of different reaction intermediates. A substantial number of studies have been conducted on the analysis and interpretation of Tafel slope values in terms of the OER mechanism. The formation of the O intermediate was previously identified as the rate-limiting step for NiFe LDH, with a Tafel slope of 64 mV dec<sup>−1</sup> in reference [46]. Similarly, the formation of HOO was identified as the rate-limiting step for NiV LDH, with a Tafel slope of 50 mV dec<sup>−1</sup>, as reported in reference [46]. The 48.4 mV dec<sup>−1</sup> Tafel slope obtained in ref. [41] was proposed to indicate that either the formation of O, HOO, or OO intermediates in steps 9, 10, and 11, respectively,

is the rate-determining step, with step 10 being the most probable. Despite the development of numerous NiFe-based catalysts, the active phase and the detailed mechanism of NiFe-based compounds remain unclear and the subject of debate. The controversy arises from the difficulty in determining the structure and pathway of OER electrocatalysis, both experimentally and theoretically [47].

The data of oxygen evolution measurements on the investigated catalysts are shown in Figure 5 and Table 3. As can be seen from the LSVs recorded on Ni and different  $\text{Ni}_x\text{Fe}_y$  catalysts in a 1 M KOH solution, the lower onset and overpotential values at  $10 \text{ mA cm}^{-2}$  were obtained on the  $\text{Ni}_x\text{Fe}_y$  catalysts containing a lower content of Ni—60 and 35 at.% and higher content of iron—40 and 65 at.% (Figure 5a). The increase in iron content in the  $\text{Ni}_x\text{Fe}_y$  coatings results in a higher activity for oxygen evolution compared with the coatings containing a lower content of iron and a higher content of nickel. The most promising composition of NiFe is Ni 60 at.% and Fe 40 at.% for efficient OER. The current density of  $10 \text{ mA cm}^{-2}$  was reached at this catalyst with an overpotential of 344.7 mV, indicating superior catalytic activity and favorable OER kinetics. The Tafel slopes obtained in our work range from 49.2 to 69.6  $\text{mV dec}^{-1}$ , indicating that the formation of the O intermediate is the most probable rate-limiting step for  $\text{Ni}_x\text{Fe}_y$  catalysts. Moreover, the oxygen evolution proceeds more easily compared with the pure Ni catalyst ( $111.2 \text{ mV dec}^{-1}$ ).

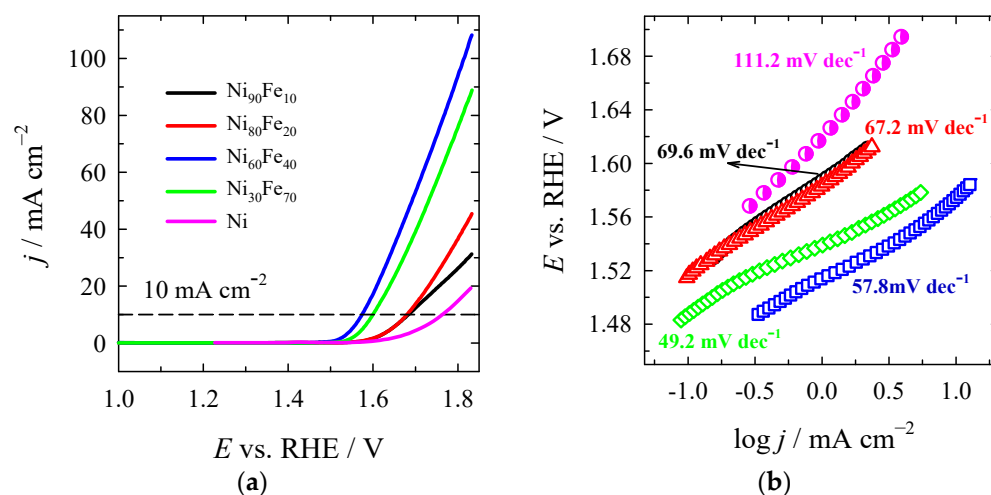


**Figure 5.** (a) The OER polarization curves of Ni,  $\text{Ni}_{90}\text{Fe}_{10}$ ,  $\text{Ni}_{80}\text{Fe}_{20}$ ,  $\text{Ni}_{60}\text{Fe}_{40}$ , and  $\text{Ni}_{35}\text{Fe}_{65}$  catalysts in  $\text{N}_2$ -saturated 1 M KOH solution at a potential scan rate of  $2 \text{ mV s}^{-1}$ ; (b) the corresponding Tafel slopes for each catalyst.

**Table 3.** The electrochemical performance of Ni and the deposited  $\text{Ni}_x\text{Fe}_y$  coatings for OER in alkaline media.

Sample	$E_{\text{onset}}$ , V at $j = 1 \text{ mA cm}^{-2}$	$\eta_{\text{onset}}$ , mV	$E$ , V at $j = 10 \text{ mA cm}^{-2}$	$\eta_{10}^*$ , mV	Tafel Slope, $\text{mV dec}^{-1}$
Ni	1.6163	386.3	1.7621	532.1	111.2
$\text{Ni}_{90}\text{Fe}_{10}$	1.5868	356.8	1.6842	454.2	69.6
$\text{Ni}_{80}\text{Fe}_{20}$	1.5829	352.9	1.6802	450.2	67.2
$\text{Ni}_{60}\text{Fe}_{40}$	1.5162	286.2	1.5747	344.7	57.8
$\text{Ni}_{35}\text{Fe}_{65}$	1.5390	309.0	1.5999	369.9	49.2

\* Overpotential at  $10 \text{ mA cm}^{-2}$ .

The distinctive yet beneficial catalytic characteristics observed in alloys, particularly in high-entropy alloys (HEAs), are attributed to the pronounced multielemental interactions [48,49]. The catalytic activity, in general, depends on various factors, including particle



size, shape, catalyst architecture, porosity, surface-area-to volume ratio, the abundance and accessibility of active sites, crystallinity, modified electronic structures, the impact of the synergistic interplay of different elements, and other factors. The determined electrocatalytic activity of the series  $\text{Ni}_x\text{Fe}_y$  alloys with varying Ni and Fe content, deposited on Cu/PI in our work, is likely dependent on the varying Ni/Fe ratios within the catalysts. In addition, there is synergistic effect between elements, which is directly related to the  $\text{O}^*$  adsorption strength. Thus, the high catalytic performance of  $\text{Ni}_{60}\text{Fe}_{40}$  can be attributed to the optimal and suitable surface Fe/Ni ratio of 1.5 for the formation of  $\text{O}^*$  intermediate and efficient OER. The crystalline structure of the  $\text{Ni}_x\text{Fe}_y$  coatings also aids in facilitating oxygen evolution. It is important to note that  $\text{Ni}_x\text{Fe}_y$  coatings completely cover the Cu layer deposited on PI surfaces. However, there is still a possibility that Cu may have a negligible yet favorable impact on the OER and HER reactions due to the fact that  $\text{Cu}^0/\text{Cu}^{\text{I}}$  is active for the HER reaction, while  $\text{Cu}^{\text{III}}$  has a high reduction potential and is the active species for the OER [50,51].

To confirm the bifunctional activity of the developed catalysts for HER and OER in alkaline media, both the cathodic (HER) (Figure 4a) and anodic (OER) (Figure 5a) polarization curves were replotted and are given in Figure 6a.

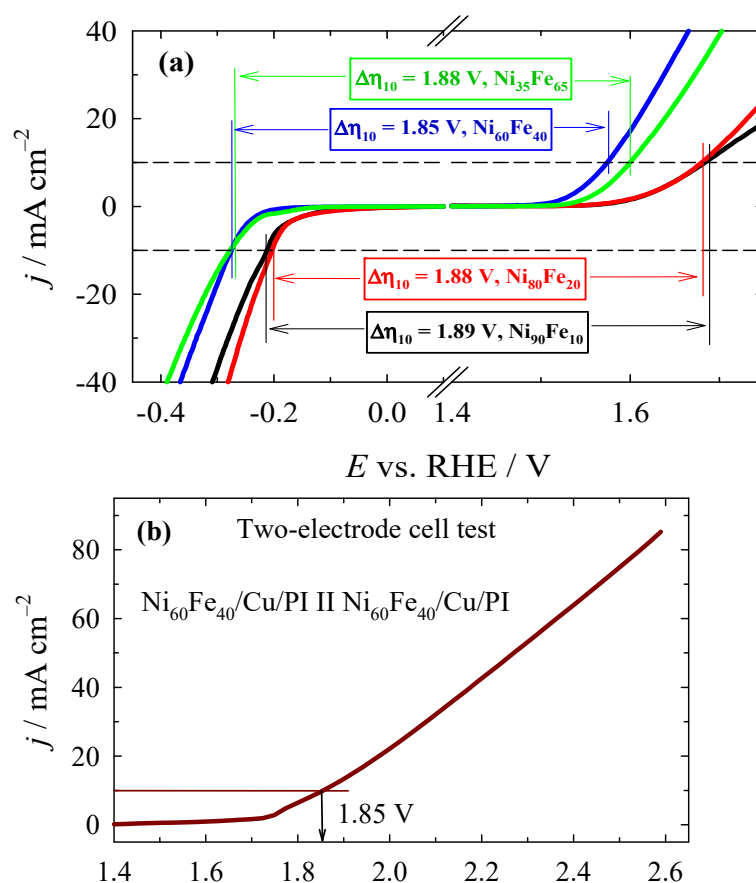


**Figure 6.** (a) The predicted bifunctional activity of  $\text{Ni}_x\text{Fe}_y$  catalysts: values of full-cell potential  $\Delta\eta_{10}$  calculated from the difference between overpotential values ( $\eta_{10}$ ) at  $\pm 10 \text{ mA cm}^{-2}$  obtained from the corresponding HER and OER LSVs in Figures 4a and 5a. (b) LSV curve for  $\text{Ni}_{60}\text{Fe}_{40}/\text{Cu}/\text{PI}$  as both anode and cathode electrocatalytic water splitting in 1 M KOH solution.

The potential difference ( $\Delta\eta_{10}$ ) between the HER and OER current density of  $\pm 10 \text{ mA cm}^{-2}$  ( $\eta_{10}^{\text{OER}} - \eta_{10}^{\text{HER}}$ ) for  $\text{Ni}_x\text{Fe}_y/\text{Cu}/\text{PI}$  catalysts represents an expected full-cell potential window. The calculated values of full-cell potential  $\Delta\eta_{10}$  delivered from the corresponding HER and OER polarization curves are 1.85 V for  $\text{Ni}_{60}\text{Fe}_{40}/\text{Cu}/\text{PI}$ , 1.88 V for  $\text{Ni}_{35}\text{Fe}_{65}/\text{Cu}/\text{PI}$  and  $\text{Ni}_{80}\text{Fe}_{20}/\text{Cu}/\text{PI}$ , and 1.89 V for  $\text{Ni}_{90}\text{Fe}_{10}/\text{Cu}/\text{PI}$  (Figure 6a). The

obtained values suggest the potential application of catalysts for a practical overall water-splitting (OWS) device in an alkaline electrolyte, employing the same electrode materials as both the anode and the cathode. The overall catalytic performance in a two-electrode alkaline electrolyzer cell configuration was also carried out by using the same Ni<sub>60</sub>Fe<sub>40</sub>/Cu/PI catalyst as both the anode and the cathode—Ni<sub>60</sub>Fe<sub>40</sub>/Cu/PI||Ni<sub>60</sub>Fe<sub>40</sub>/Cu/PI. The developed Ni<sub>60</sub>Fe<sub>40</sub>/Cu/PI electrode exhibits a cell potential of 1.85 V at 10 mA cm<sup>-2</sup> (Figure 6b) compared to other cell potential values reported in the literature—Ni-Fe/Cu||Ni-Fe/Cu (1.83 V) [17] and NiO@CNTR||NiO@CNTR (1.81 V) [52] as well as being comparable with the Pt/C||IrO<sub>2</sub> (1.71 V) and Pt/C||Pt/C (1.83 V) [53]. The calculated energy efficiency of the Ni<sub>60</sub>Fe<sub>40</sub>/Cu/PI cell is 66.5%. Moreover, the turnover frequency (TOF) is an important indicator for the determination of the intrinsic activity of the catalysts. Herein, the TOF values were calculated to evaluate the intrinsic OER performance of the prepared Ni<sub>x</sub>Fe<sub>y</sub>/Cu/PI catalysts at an overpotential of 600 mV. The TOF value of Ni<sub>60</sub>Fe<sub>40</sub>/Cu/PI catalyst was observed as 14.9 s<sup>-1</sup> at an overpotential of 600 mV, which significantly outperforms that of Ni<sub>35</sub>Fe<sub>65</sub>/Cu/PI (9.3 s<sup>-1</sup>), Ni<sub>90</sub>Fe<sub>10</sub>/Cu/PI (1.9 s<sup>-1</sup>), and Ni<sub>80</sub>Fe<sub>20</sub>/Cu/PI (1.8 s<sup>-1</sup>), indicating the high intrinsic properties of this catalyst. The results of our study offer insights into the future design of flexible composite electrocatalysts for sustainable hydrogen production. Furthermore, the suggested strategy allows us to produce low-cost, scalable, and self-standing electrocatalysts with efficient water-splitting activity and stability.

### 3. Materials and Methods

#### 3.1. Chemicals

Nickel sulfate (NiSO<sub>4</sub>·7H<sub>2</sub>O, >98%, Chempur, Piekary Śląskie, Poland), iron sulfate heptahydrate (FeSO<sub>4</sub>·7H<sub>2</sub>O, 97%, Chempur, Piekary Śląskie, Poland), morpholine borane (MB, C<sub>4</sub>H<sub>8</sub>ONH·BH<sub>3</sub>, 97%, Alfa Aesar, Kandel, Germany), glycine (NH<sub>2</sub>CH<sub>2</sub>COOH, 99%, Chempur, Piekary Śląskie, Poland), ethylenediaminetetraacetic acid (EDTA, 99%, Reachem, San Miguel, Chile), sodium malonate (CH<sub>2</sub>(COONa)<sub>2</sub>, 97%, Merck SA, Athens, Greece), palladium chloride (PdCl<sub>2</sub>, 59.5%, Thermo Fisher Scientific, United Kingdom), copper sulfate pentahydrate (CuSO<sub>4</sub>·5H<sub>2</sub>O, 98%, Chempur, Piekary Śląskie, Poland), sulfuric acid (H<sub>2</sub>SO<sub>4</sub>, 98%, Chempur, Piekary Śląskie, Poland), and polyimide (PI) film of 0.125 mm thickness (DuPont™ Kapton® HN, GoodFellow Cambridge Limited, Huntingdon, England) were used.

#### 3.2. Electroless Plating of NiFe Coatings on Polyimide Coated with Cu Film

Before the electroless plating of NiFe coatings, the PI surface was pre-treated using adhesion/activation pretreatment procedures as described in detail in refs. [54,55]. The Cu layer was electroplated from CuSO<sub>4</sub> and H<sub>2</sub>SO<sub>4</sub> solution at a current density of 1 A dm<sup>-2</sup> for 45 min. Then, the NiFe coatings with different contents of Ni and Fe were deposited on the Cu-coated PI surface using electroless metal plating, with morpholine borane as the reducing agent. Figure 7 shows the scheme of the plating process of Ni<sub>x</sub>Fe<sub>y</sub> on Cu/PI.

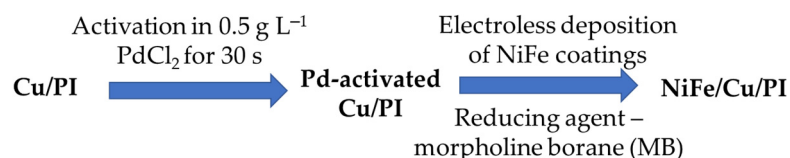


**Figure 7.** The scheme of the plating process of NiFe on Cu/PI.

Briefly, the Cu/PI surface was activated with Pd<sup>2+</sup> ions by immersion it in a 0.5 g L<sup>-1</sup> PdCl<sub>2</sub> solution for 30 s, then rinsed with deionized water and placed in a freshly prepared electroless plating solution. The composition of the electroless plating solution and the deposition parameters of the coatings are given in Table 4.

**Table 4.** The composition of the electroless plating solution and the plating parameters of NiFe coatings on the Cu/PI surface.

Sample	Composition of Plating Solution, M						Plating Conditions		
	NiSO <sub>4</sub>	MB	NH <sub>2</sub> CH <sub>2</sub> COOH	FeSO <sub>4</sub>	EDTA	CH <sub>2</sub> (COONa) <sub>2</sub>	pH	T, °C	t, Min
No. 1				0.01					
No. 2	0.14	0.2	0.2	0.005	0.05	0.1	7	60	60
No. 3				0.001					
No.4				0.0005					

In all cases, the pH of the plating solutions was 7 (measured at room temperature). The plating bath was operated at a temperature of 60 °C for 60 min (Table 4). Concentrations of glycine, nickel sulfate, ethylenediaminetetraacetic acid, and sodium malonate were kept constant, whereas the concentration of iron sulfate was different.

### 3.3. Characterization of Coatings

The composition of the NiFe coatings deposited on the Cu surface was determined using inductively coupled plasma–optical emission spectroscopy (ICP-OES). The Ni and Fe loadings in the coatings were determined using an Optima 7000DV ICP spectrometer (PerkinElmer, Shelton, CT, USA).

The surface morphology of the samples and the distribution of elements were analyzed using a TM4000Plus scanning electron microscope with an AZetecOne detector (Hitachi, Tokyo, Japan).

The XRD patterns of the investigated samples were measured using an X-ray diffractometer D2 PHASER (Bruker, Karlsruhe, Germany). The measurements were performed in the 2θ range of 10–90°.

### 3.4. Electrochemical Measurements of HER and OER

The performance of the synthesized samples was evaluated using a PGSTAT100 potentiostat/galvanostat (Metrohm Autolab B. V., Utrecht, The Netherlands). A standard three-electrode cell was used, where the working electrode was NiFe/Cu/PI with a geometric surface area of 2 cm<sup>2</sup>. The reference and counter electrodes were Ag/AgCl (3 M KCl) and glassy carbon (GC), respectively. Linear sweep voltammograms (LSVs) were recorded in an N<sub>2</sub>-saturated 1 M KOH solution at a scan rate of 2 mV s<sup>−1</sup>. For comparison, a Ni foam electrode (2 cm<sup>2</sup>) was used. All reported potential values were referred to the reversible hydrogen electrode (*E*<sub>RHE</sub>) according to the following Equation (12):

$$E_{\text{RHE}} = E_{\text{measured}} + 0.059 \cdot \text{pH} + E_{\text{Ag/AgCl (3 M KCl)}} \quad (12)$$

where  $E_{\text{Ag/AgCl (3 M KCl)}} = 0.210 \text{ V}$ .

The HER and OER current densities presented in this paper have been scaled to the geometric area of the catalysts.

A two-electrode water electrolysis cell was constructed using two of the same Ni<sub>60</sub>Fe<sub>40</sub>/Cu/PI electrodes as the anode and the cathode. The energy efficiency of the cell was calculated using the following equation:

$$\eta_{\text{electrolyzer}} = E_{\text{th}}/V_{\text{e at } j} \quad (13)$$

where  $E_{\text{th}} = 1.23 \text{ V}$ ;  $V_{\text{e at } j}$  is the input voltage required to drive the electrolysis at the current density of interest. The energy efficiency calculated in this study was obtained at  $j = 10 \text{ mA cm}^{-2}$ .

The turnover frequency (TOF) value was calculated using the following Equation (14) [56]:

$$\text{TOF} = j \times A/4 \times F \times n \quad (14)$$

where  $j$  is the current density at an overpotential of 600 mV,  $A$  is the geometric surface area of the electrode,  $F$  is the Faraday constant ( $96,485 \text{ C mol}^{-1}$ ),  $4$  is the number of electrons transferred in the OER, and  $n$  is the number of moles of all metal ions calculated from the ICP-OES results.

#### 4. Conclusions

In this study, we highlighted a promising strategy to fabricate cost-effective and flexible catalysts for electrochemical water-splitting devices. NiFe coatings containing different contents of Ni and Fe have been plated on the flexible copper-coated polyimide surface using the low-cost and straightforward electroless metal-plating method and morpholine borane as a reducing agent. It was found that the most promising catalysts for HER and OER are Ni<sub>80</sub>Fe<sub>20</sub>/Cu/PI and Ni<sub>60</sub>Fe<sub>40</sub>/Cu/PI catalysts, respectively. The Ni<sub>80</sub>Fe<sub>20</sub>/Cu/PI catalyst exhibited the lowest overpotential value of  $-202.7 \text{ mV}$  for the HER to obtain a current density of  $10 \text{ mA cm}^{-2}$ , while the lowest OER overpotential ( $344.7 \text{ mV}$ ) was observed for the Ni<sub>60</sub>Fe<sub>40</sub>/Cu/PI catalyst to obtain a current density of  $10 \text{ mA cm}^{-2}$ . A cell potential of  $1.85 \text{ V}$  at  $10 \text{ mA cm}^{-2}$  was achieved by employing the developed flexible Ni<sub>60</sub>Fe<sub>40</sub>/Cu/PI catalyst as the anode and the cathode (Ni<sub>60</sub>Fe<sub>40</sub>/Cu/PI||Ni<sub>60</sub>Fe<sub>40</sub>/Cu/PI). The exploration of the bifunctional electrocatalysts for overall water splitting by Ni<sub>x</sub>Fe<sub>y</sub> deposited on Cu-coated polyimide provides insights into the future design of composite electrocatalysts for the production of hydrogen via electrochemical water splitting.

**Author Contributions:** Conceptualization, L.T.-T. and E.N.; methodology, D.S.; validation, Z.S., J.V. and B.Š.-S.; formal analysis, A.B., A.N. and Z.S.; investigation, D.S., A.B., A.N., B.Š.-S. and J.V.; data curation, J.V., B.Š.-S. and A.N.; writing—original draft preparation, L.T.-T. and D.Š.; writing—review and editing, E.N. and D.Š.; visualization, A.N., B.Š.-S. and A.B.; supervision, L.T.-T.; project administration, L.T.-T.; funding acquisition, L.T.-T. All authors have read and agreed to the published version of the manuscript.

**Funding:** This research was funded by a grant (No. P-MIP-23-467) from the Research Council of Lithuania.

**Institutional Review Board Statement:** Not applicable.

**Data Availability Statement:** Data are contained within the article.

**Conflicts of Interest:** The authors declare no conflicts of interest.

#### References

1. Gong, Y.; Yao, J.; Wang, P.; Li, Z.; Zhou, H.; Xu, C. Perspective of hydrogen energy and recent progress in electrocatalytic water splitting. *Chin. J. Chem. Eng.* **2022**, *43*, 282–296. [[CrossRef](#)]
2. Hota, P.; Das, A.; Maiti, D.K. A short review on generation of green fuel hydrogen through water splitting. *Int. J. Hydrogen Energy* **2023**, *48*, 523–541. [[CrossRef](#)]
3. Elsapagh, R.M.; Sultan, N.S.; Mohamed, F.A.; Fahmy, H.M. The role of nanocatalysts in green hydrogen production and water splitting. *Int. J. Hydrogen Energy* **2024**, *67*, 62–82. [[CrossRef](#)]
4. Solanki, R.; Patra, I.; Ahmad, N.; Kumar, N.B.; Parra, R.M.R.; Zaidi, M.; Yasin, G.; Kumar, T.C.A.; Hussein, H.A.; Sivaraman, R.; et al. Investigation of recent progress in metal-based materials as catalysts toward electrochemical water splitting. *J. Environ. Chem. Eng.* **2022**, *10*, 108207. [[CrossRef](#)]
5. Sun, H.; Xu, X.; Chen, G.; Shao, Z. Perovskite oxides as electrocatalysts for water electrolysis: From crystalline to amorphous. *Carbon Energy* **2024**, e595. [[CrossRef](#)]
6. Carmo, M.; Fritz, D.L.; Mergel, J.; Stolten, D.A. Comprehensive review on PEM water electrolysis. *Int. J. Hydrogen Energy* **2013**, *38*, 4901–4934. [[CrossRef](#)]
7. Chao, T.; Hu, Y.; Hong, X.; Li, Y. Design of noble metal electrocatalysts on an atomic level. *ChemElectroChem* **2019**, *6*, 289–303. [[CrossRef](#)]
8. Liu, G.; Hou, F.; Wang, X.; Fang, B. Ir-IrO<sub>2</sub> with heterogeneous interfaces and oxygen vacancies-rich surfaces for highly efficient oxygen evolution reaction. *Appl. Surf. Sci.* **2023**, *615*, 156333. [[CrossRef](#)]
9. Yang, Y.; Zhou, T.; Zeng, Z.; Hu, Y.; Yang, F.; Sun, W.; He, L. Novel sulfate solid supported binary Ru-Ir oxides for superior electrocatalytic activity towards OER and CER. *J. Colloid. Interface Sci.* **2024**, *659*, 191–202. [[CrossRef](#)]
10. Zeng, H.; Ji, Y.; Wen, J.; Li, X.; Zheng, T.; Jiang, Q.; Xia, C. Pt nanocluster-catalyzed hydrogen evolution reaction: Recent advances and future Outlook. *Chin. Chem. Lett.* **2024**, 109686. [[CrossRef](#)]

11. Li, X.-P.; Huang, C.; Han, W.-K.; Ouyang, T.; Liu, Z.-Q. Transition metal-based electrocatalysts for overall water splitting. *Chin. Chem. Lett.* **2021**, *32*, 2597–2616. [[CrossRef](#)]
12. Li, Z.; Zhang, X.; Ou, C.; Zhang, Y.; Wang, W.; Dong, S.; Dong, X. Transition metal-based self-supported anode for electrocatalytic water splitting at a large current density. *Coord. Chem. Rev.* **2023**, *495*, 215381. [[CrossRef](#)]
13. Li, Y.; Zhou, L.; Guo, S. Noble metal-free electrocatalytic materials for water splitting in alkaline electrolyte. *EnergyChem* **2021**, *3*, 100053. [[CrossRef](#)]
14. Wang, X.; Yu, X.; Bai, J.; Yuan, G.; He, P.; Zhu, Y.; Wu, S.; Qin, F.; Ren, L. Interface engineering assisted Fe-Ni<sub>3</sub>S<sub>2</sub>/Ni<sub>2</sub>P heterostructure as a high-performance bifunctional electrocatalyst for OER and HER. *Electrochim. Acta* **2023**, *458*, 142524. [[CrossRef](#)]
15. Sun, S.; Zhang, C.; Ran, M.; Zheng, Y.; Li, C.; Jiang, Y.; Yan, X. Fe-doped promotes phosphorization and dispersibility of Ni catalysts for efficient and stable HER and OER. *Int. J. Hydrogen Energy* **2024**, *63*, 133–141. [[CrossRef](#)]
16. Liu, Y.; Ma, X.; Huang, H.; Deng, G.; Wang, J.; Chen, X.; Gao, T. Ammonia-assisted Ni particle preferential deposition in Ni-Fe pyrophosphates on iron foam to improve the catalytic performance for overall water splitting. *J. Colloid Interf. Sci.* **2024**, *665*, 573–581. [[CrossRef](#)]
17. Xu, W.; Qiu, R.; Mao, X.; Yan, X.; Peng, B.; Shen, Y. One-step fabrication of amorphous Ni-Fe phosphated alloys as efficient bifunctional electrocatalysts for overall water splitting. *J. Non-Cryst. Solids* **2022**, *587*, 121598. [[CrossRef](#)]
18. Liu, S.; Wang, Y.; Gao, J.; Jin, W.; Xiao, W.; Xin, L.; Xiao, Z.; Xu, G.; Dai, C.; Zhang, H.; et al. Anionic phosphorous and sulfur regulate self-supported Ni-Fe-based electrocatalyst for water-splitting under large current density. *Fuel* **2024**, *367*, 131445. [[CrossRef](#)]
19. Han, P.; Tan, T.; Wu, F.; Cai, P.; Cheng, G.; Luo, W. Nickel-iron borate coated nickel-iron boride hybrid for highly stable and active oxygen evolution electrocatalysis. *Chin. Chem. Lett.* **2020**, *31*, 2469–2472. [[CrossRef](#)]
20. Dai, Z.; Du, X.; Zhang, X. The synthesis of Ni-Co-Fe-Se@NiCo-LDH nanoarrays on Ni foam as efficient overall water splitting electrocatalyst. *J. Alloys Compd.* **2023**, *946*, 169451. [[CrossRef](#)]
21. Shi, Y.; Li, C.; Tu, Y.; Jiang, Y.; Xiao, W.; Zhu, S.; Lv, P.; Yan, X. Surface reconstruction of Fe doping NiC<sub>2</sub>O<sub>4</sub> by the electrocatalytic reaction to improve the performance of overall water splitting. *Ceram. Int.* **2024**, *50*, 36340–36348. [[CrossRef](#)]
22. Lu, P.; Zhao, H.; Jiang, X.; Yang, L.; Xie, G.; Xie, T.; Jiang, L. Electroless deposition synthesis of composite catalysts Ni-Fe-P-Ni(OH)<sub>2</sub>/NF with superior overall water splitting performance. *J. Environ. Chem. Eng.* **2024**, *12*, 114039. [[CrossRef](#)]
23. Zeng, L.; Yang, L.; Lu, J.; Jia, J.; Yu, J.; Deng, Y.; Shao, M.; Zhou, W. One-step synthesis of Fe-Ni hydroxide nanosheets derived from bimetallic foam for efficient electrocatalytic oxygen evolution and overall water splitting. *Chin. Chem. Lett.* **2018**, *29*, 1875–1878. [[CrossRef](#)]
24. Xiao, M.; Jiao, L.; Xiang, D.; Gao, P.; Fu, J.; Naseri, A.; Huang, S. Synergistic electronic structure tuning of self-assembled hollow hierarchical Ni-Fe-Co-P nanowire arrays on carbon cloth for enhanced water splitting. *J. Alloys Compd.* **2023**, *968*, 171883. [[CrossRef](#)]
25. Shao, S.; Li, X.; Guo, R.; Wang, J.; Sheng, M. Ni-Fe-P nanoparticles encapsulated in carbon nanotubes supported on carbon cloth for overall water splitting. *Mater. Lett.* **2023**, *352*, 135204. [[CrossRef](#)]
26. Shin, Y.; Cho, S.C.; Park, G.; Seol, J.H.; Lim, D.; Choi, S.; Jo, C.; Baeck, S.H.; Lim, J.; Lee, S.U.; et al. Atomic-level insights into bioinspired Fe/Ni bimetallic active sites on carbon nitrides for electrocatalytic O<sub>2</sub> evolution. *J. Chem. Eng.* **2024**, *85*, 149799. [[CrossRef](#)]
27. Kalusulingam, R.; Ravi, K.; Mathi, S.; Yadhav, N.; Mikheykin, A.S.; Biradar, A.V.; Srinivasan, K.; Myasoedova, T.N. Bimetallic Ni-Fe nanoparticles encapsulated with biomass-derived N-doped graphitic carbon core-shell nanostructures an efficient bifunctional electrocatalyst for enhanced overall seawater splitting and human urine electrolysis. *Mater. Today Sustain.* **2024**, *27*, 100864. [[CrossRef](#)]
28. Abdelrahim, A.M.; El-Moghny, M.G.A.; El-Deab, M.S. Interface construction of Ni(OH)<sub>2</sub>/Fe<sub>3</sub>O<sub>4</sub> heterostructure decorating in-situ defected graphite felt for enhanced overall water splitting. *Int. J. Hydrogen Energy* **2024**, *81*, 173–186. [[CrossRef](#)]
29. Ning, F.; He, X.; Shen, Y.; Jin, H.; Li, Q.; Li, D.; Li, S.; Zhan, Y.; Du, Y.; Jiang, J.; et al. Flexible and lightweight fuel cell with high specific power density. *ACS Nano* **2017**, *11*, 5982–5991. [[CrossRef](#)]
30. Kim, T.; Lee, J.; Kim, N.; Lee, S.; Gu, M.; Kim, B.-S. Redox-active polyimides for energy conversion and storage: From synthesis to application. *Chem. Commun.* **2023**, *59*, 153–169. [[CrossRef](#)]
31. Li, X.; Wang, T.; Wang, C. An advanced flower-like Co-Ni/PI-CNT film electrocatalyst for oxygen evolution reaction. *J. Alloys Compd.* **2017**, *729*, 19–26. [[CrossRef](#)]
32. Zhang, L.; Bai, J.; Zhang, S.; Liu, Y.; Ye, J.; Fan, W.; Debroye, E.; Liu, T. Atomically dispersed iridium on polyimide support for acidic oxygen evolution. *ACS Nano* **2024**, *18*, 22095–22103. [[CrossRef](#)]
33. Wang, T.; Li, X.; Jiang, Y.; Zhou, Y.; Jia, L.; Wang, C. Reduced graphene oxide-polyimide/carbon nanotube film decorated with NiSe nanoparticles for electrocatalytic hydrogen evolution reactions. *Electrochim. Acta* **2017**, *243*, 291–298. [[CrossRef](#)]
34. Xie, Y.; Zhang, C.; He, X.; White, T.; Demaree, J.D.; Griep, M.; Lina, J. Monolithic electrochemical cells for overall water splitting. *J. Power Sources* **2018**, *397*, 37–43. [[CrossRef](#)]
35. McGovern, M.S.; Garnett, E.C.; Rice, C.; Masel, R.I.; Wieckowski, A. Effects of Nafion as a binding agent for unsupported nanoparticle catalysts. *J. Power Sources* **2003**, *115*, 35–39. [[CrossRef](#)]



36. Liu, H.; Wang, X.; Antwi-Afari, M.F.; Mi, H.-Y.; Liu, C. A state-of-the-art review of polyimide foams research. *Constr. Build. Mater.* **2024**, *437*, 136961. [[CrossRef](#)]
37. Jing, P.; Liu, M.; Pu, Y.; Cui, Y.; Wang, Z.; Wang, J.; Liu, Q. Dependence of phase configurations, microstructures and magnetic properties of iron-nickel (Fe-Ni) alloy nanoribbons on deoxidization temperature in hydrogen. *Sci. Rep.* **2016**, *6*, 37701. [[CrossRef](#)]
38. Chenna, A.; Benbrahim, N.; Hamadou, L.; Boudinar, S.; Kadri, A.; Chainet, E.; Dahmane, Y. Characterisation of electroplated Ni<sub>45</sub>Fe<sub>55</sub> thin films on n-Si (111). *Surf. Eng.* **2018**, *35*, 189–198. [[CrossRef](#)]
39. Zhu, G.X.; Lu, T.L.; Han, L.; Zhan, Y.Z. Graphitic carbon nitride (g-C<sub>3</sub>N<sub>4</sub>) as an efficient metal-free Fenton-like catalyst for degrading organic pollutants: The overlooked non-photocatalytic activity. *Water Sci. Technol.* **2020**, *81*, 518–528. [[CrossRef](#)]
40. Gong, M.; Wang, D.Y.; Chen, C.-C.; Hwang, B.-J.; Dai, H. A mini review on nickel-based electrocatalysts for alkaline hydrogen evolution reaction. *Nano Res.* **2016**, *9*, 28–46. [[CrossRef](#)]
41. Alobaid, A.; Wang, C.; Adomaitis, R.A. Mechanism and kinetics of HER and OER on NiFe LDH films in an alkaline electrolyte. *J. Electrochem. Soc.* **2018**, *165*, J3395–J3404. [[CrossRef](#)]
42. Bodhankar, P.M.; Sarawade, P.B.; Singh, G.; Vinu, A.; Dhawale, D.S. Recent advances in highly active nanostructured NiFe LDH catalyst for electrochemical water splitting. *Mater. Chem. A* **2021**, *9*, 3180. [[CrossRef](#)]
43. Bao, F.; Kempainen, E.; Dorbandt, I.; Xi, F.; Bors, R.; Maticic, N.; Wenisch, R.; Bagacki, R.; Schary, C.; Michalczyk, U.; et al. Host, suppressor, and promoter—The roles of Ni and Fe on oxygen evolution reaction activity and stability of NiFe alloy thin films in alkaline media. *ACS Catal.* **2021**, *11*, 10537–10552. [[CrossRef](#)]
44. Bian, H.; Chen, T.; Chen, Z.; Liu, J.; Li, Z.; Du, P.; Zhou, B.; Zeng, X.; Tang, J.; Liu, C. One-step synthesis of mesoporous cobalt sulfides (CoS<sub>x</sub>) on the metal substrate as an efficient bifunctional electrode for overall water splitting. *Electrochim. Acta* **2021**, *389*, 138786. [[CrossRef](#)]
45. Trotochaud, L.; Ranney, J.K.; Williams, K.N.; Boettcher, S.W. Solution-cast metal oxide thin film electrocatalysts for oxygen evolution. *J. Am. Chem. Soc.* **2012**, *134*, 17253–17261. [[CrossRef](#)]
46. Fan, K.; Chen, H.; Ji, Y.; Huang, H.; Claesson, P.M.; Daniel, Q.; Philippe, B.; Rensmo, H.; Li, F.; Luo, Y.; et al. Nickel-vanadium monolayer double hydroxide for efficient electrochemical water oxidation. *Nat Commun.* **2016**, *7*, 11981. [[CrossRef](#)]
47. Gong, M.; Dai, H. A mini review of NiFe-based materials as highly active oxygen evolution reaction electrocatalysts. *Nano Res.* **2015**, *8*, 23–39. [[CrossRef](#)]
48. Sun, Y.; Dai, S. High-entropy materials for catalysis: A new frontier. *Sci. Adv.* **2021**, *7*, eabg1600. [[CrossRef](#)]
49. Xu, X.; Shao, Z.; Jiang, S.P. High-Entropy Materials for Water Electrolysis. *Energy Technol.* **2022**, *10*, 2200573. [[CrossRef](#)]
50. Luo, C.; Liu, X.; Yang, K.; Xu, J.; Zhu, Z.; Tang, Z.; Shen, S.; Fan, J.; Luo, D.; Alshammari, N.; et al. Coordination structure engineering of Cu-based electrocatalysts for electrocatalytic water splitting. *Coord. Chem. Rev.* **2024**, *516*, 215936. [[CrossRef](#)]
51. Rajput, A.; Kundu, A.; Chakraborty, B. Recent progress on copper-based electrode materials for overall water-splitting. *ChemElectroChem* **2021**, *8*, 1698–1722. [[CrossRef](#)]
52. Ganguly, A.; McGlynn, R.J.; Boies, A.; Maguire, P.; Mariotti, D.; Chakrabarti, S. Flexible bifunctional electrode for alkaline water splitting with long-term stability. *ACS Appl. Mater. Interf.* **2024**, *16*, 12339–12352. [[CrossRef](#)]
53. Jiao, L.; Zhou, Y.X.; Jiang, H.L. Metal-organic framework-based CoP/reduced graphene oxide: High-performance bifunctional electrocatalyst for overall water splitting. *Chem. Sci.* **2016**, *7*, 1690–1695. [[CrossRef](#)]
54. Naruškevičius, L.; Tamašauskaitė-Tamašiūnaitė, L.; Žielienė, A.; Jasulaitienė, V. A Co-based surface activator for electrodeless copper deposition. *Surf. Coat. Technol.* **2012**, *206*, 2967–2971. [[CrossRef](#)]
55. Hyman, M.; Naruškevičius, L.; Budilovskis, D. Chrome-Free Adhesion Pre-Treatment for Plastics. US10920321B2, 16 February 2021.
56. Zhou, T.; Cao, Z.; Zhang, P.; Ma, H.; Gao, Z.; Wang, H.; Lu, Y.; He, J.; Zhao, Y. Transition metal ions regulated oxygen evolution reaction performance of Ni-based hydroxides hierarchical nanoarrays. *Sci. Rep.* **2017**, *7*, 46154. [[CrossRef](#)]

**Disclaimer/Publisher's Note:** The statements, opinions and data contained in all publications are solely those of the individual author(s) and contributor(s) and not of MDPI and/or the editor(s). MDPI and/or the editor(s) disclaim responsibility for any injury to people or property resulting from any ideas, methods, instructions or products referred to in the content.